

Scoring Molecular Wires Subject to an Ultra-Fast Laser Pulse for Molecular Electronic Devices

Hui Lu¹, Alireza Azizi², Xiao Peng Mi¹, Yu Wenjing¹, Yuting Peng¹, Tianlv Xu¹, Herbert Früchtl³, Tanja van Mourik³,
Steven R. Kirk^{*1} and Samantha Jenkins^{*1}

¹Key Laboratory of Chemical Biology and Traditional Chinese Medicine Research and Key Laboratory of Resource National and Local Joint Engineering Laboratory for New Petro-chemical Materials and Fine Utilization of Resources, College of Chemistry and Chemical Engineering, Hunan Normal University, Changsha, Hunan 410081, China.

²State Key Laboratory of Powder Metallurgy, School of Materials Science & Engineering, Central South University, Changsha, Hunan 410083, China

³EaStCHEM School of Chemistry, University of Saint Andrews, North Haugh, St Andrews, Fife KY16 9ST, Scotland, United Kingdom.

email: steven.kirk@cantab.net

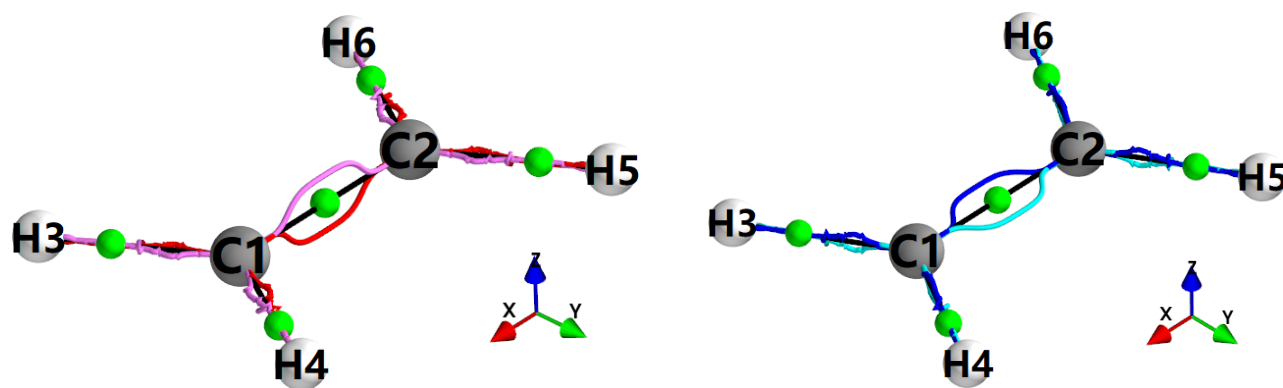
email: samanthajsuman@gmail.com

A non-ionizing ultra-fast laser pulse of 20 femtosecond duration with a peak amplitude electric-field $\pm E = 200 \times 10^{-4}$ a.u. was simulated. It was applied to the ethene molecule to consider its effect on the electron dynamics, both during the application of the laser pulse and for up to 100 femtoseconds after the pulse was switched off. Four laser pulse frequencies $\omega = 0.2692$ a.u., 0.2808 a.u., 0.2830 a.u. and 0.2900 a.u. were chosen to correspond to excitation energies mid-way between the (S_1, S_2), (S_2, S_3), (S_3, S_4) and (S_4, S_5) electronic states, respectively. Scalar quantum theory of atoms in molecules (QTAIM) was used to quantify the shifts of the C1-C2 bond critical points (BCPs). Depending on the frequencies ω selected, the C1-C2 BCP shifts were up to 5.8 times higher after the pulse was switched off compared with a static E -field with the same magnitude. Next generation QTAIM (NG-QTAIM) was used to visualize and quantify the directional chemical character. In particular polarization effects and bond strengths, in the form of bond-rigidity vs. bond-flexibility, were found, for some laser pulse frequencies, to increase after the laser pulse was switched off. Our analysis demonstrates that NG-QTAIM, in partnership with ultra-fast laser irradiation, is useful as a tool in the emerging field of ultra-fast electron dynamics which will be essential for the design and control of molecular electronic devices.

Introduction

The miniaturization of semiconductor devices according to Moore's Law [1] is reaching its physical limits. Therefore, the creation of electronic devices from individual atoms or molecules is the defining goal of electronics [2]. Towards this end, the single-molecule-junction research field is attracting increased interest [3]. In particular properties of conjugated carbon -C=C- 'linkages', as wires between building blocks, have prompted a huge and diverse body of research in polyenes, cumulenes and related molecular motifs [4]–[10]. Ethene in particular has attracted a substantial body of both theoretical and experimental research investigations [11]–[24] focusing on excited state photo-dynamics, as it is the repeating unit of the simplest polyene and the smallest organic molecule that comprises a π orbital.

Oriented static electric (\mathbf{E})-fields can significantly alter the potential energy surfaces (PES) of molecules in terms of bond breaking and bond making processes for the control of chemical reactions [25]–[31]. Using strong external homogenous \mathbf{E} -fields ($\pm 10 \times 10^9 \text{ Vm}^{-1}$), Sowlati-Hashjin and Matta discovered that parallel \mathbf{E} -fields increasingly stretch a bond with increasing \mathbf{E} -field strength; conversely, antiparallel fields compress the bond but to a lesser extent [32]. Previously for the ethene molecule, we used static \mathbf{E} -fields in the range $\pm 100 \times 10^{-4} \text{ a.u.}$ ($\approx \pm 5.14 \times 10^9 \text{ Vm}^{-1}$) to $\pm 200 \times 10^{-4} \text{ a.u.}$ ($\approx \pm 10.28 \times 10^9 \text{ Vm}^{-1}$), which are easily accessible within a Scanning Tunneling Microscope (STM) [33]. Knowledge of the energy barrier only enabled an understanding of the energetics of the switch, but did not return directional information on the effect of varying the direction or orientation of the applied \mathbf{E} -field. This was because of the presence of only very slight changes to the molecular geometry. Therefore, only subtle changes to the QTAIM properties were observed including the shift of the C-C and C-H bond critical points ($BCPs$ s) and a change to the ellipticity ε ($\approx 2\%$). These BCP shifts demonstrated polarization through a change in the atomic boundaries and therefore size of the atoms involved in a bond. More substantial changes were found using vector-based NG-QTAIM [34] in the form of polarization effects observed from changes to the morphology of the 3-D envelope around the BCP , see **Scheme 1**.



Scheme 1. The ethene bond-path framework set \mathbb{B} displaying the $\{q(\text{magenta}), q'(\text{red})\}$ path-packets for the most preferred directions of charge density accumulation $\rho(\mathbf{r})$ of the relaxed geometry (left-panel), with the corresponding least preferred directions of $\rho(\mathbf{r})$: $\{p(\text{blue}), p'(\text{cyan})\}$ path-packets (right-panel). The green spheres indicate the locations of the $BCPs$, notice the x, y, z Cartesian coordinate axes.

In this investigation, we will consider the effect of the electron dynamics exclusively and not processes that involve any shifting of nuclear positions that may occur during the formation and rupture of chemical bonds [35]–[39]. We will use NG-QTAIM’s directional interpretation of bonding, incorporating the *most* and *least* preferred directions of electronic charge density accumulation $\rho(\mathbf{r})$ using ethene as the molecular wire [40], see **Scheme 1**. The main goal of this investigation is to obtain the basic principles governing the effect of an ultra-fast non-ionizing laser pulse on the electronic charge density distribution, compared to the static **E**-field that we previously undertook. This will involve using NG-QTAIM to quantify the effect of an ultra-fast non-ionizing laser pulse on the electron dynamics of ethene in the complete absence of nuclear motion. Because an ultra-fast pulse will create an energetic broadening of the basic laser frequency, a number of laser frequencies spanning the lower-lying excited states will be investigated, see the Computational Details section.

2. Theory and Methods

2.1 The QTAIM and BCP descriptors; ellipticity ε

The four types of QTAIM [41] critical points are labelled using the notation (R, ω) , where R is the rank of the Hessian matrix and ω is the signature corresponding to the algebraic sum of the signs of the eigenvalues. These critical points can be divided into four types of topologically stable critical points according to the set of ordered eigenvalues $\lambda_1 < \lambda_2 < \lambda_3$, with corresponding eigenvectors $\underline{\mathbf{e}}_1$, $\underline{\mathbf{e}}_2$, $\underline{\mathbf{e}}_3$ of the Hessian matrix. The (3, -3) [nuclear critical point (*NCP*), a local maximum], (3, -1) and (3, 1) [saddle points, referred to as bond critical points (*BCP*) and ring critical points (*RCP*), respectively] and (3, 3) [the cage critical points (*CCP*)]. QTAIM allows us to identify critical points in the total electronic charge density distribution $\rho(\mathbf{r})$ by analyzing the gradient vector field $\nabla\rho(\mathbf{r})$. In the limit that the forces on the nuclei become vanishingly small, an atomic interaction line (AIL) [42] becomes a bond-path, which may not be a chemical bond [43]. The full set of critical points and the associated bond-paths of a molecule/cluster are referred to as the molecular graph. The ellipticity $\varepsilon = |\lambda_1|/|\lambda_2| - 1$, where λ_1 and λ_2 are negative eigenvalues of the corresponding $\underline{\mathbf{e}}_1$ and $\underline{\mathbf{e}}_2$, respectively, provides the relative accumulation of $\rho(\mathbf{r}_b)$ in the two directions perpendicular to the bond-path at a *BCP*. The associated eigenvectors $\underline{\mathbf{e}}_1$ and $\underline{\mathbf{e}}_2$ correspond to the least and most preferred directions of charge density accumulation $\rho(\mathbf{r}_b)$, and the $\underline{\mathbf{e}}_3$ eigenvector is always directed along the bond path.

The C1-C2 *BCP* shifts $\Delta(\text{C1-BCP}, \text{BCP-C2})$ are calculated as the difference in partial bond-lengths measured with and without the presence of the laser pulse as a function of the **E**-field direction, $\text{C1} \rightarrow \text{C2}$ ($-\mathbf{E}_x$) or $\text{C1} \leftarrow \text{C2}$ ($+\mathbf{E}_x$) and frequency of the laser pulse, see **Scheme 1** for the direction of the Cartesian **x** axis. The shift in the C1-C2 *BCP* position is tracked for up to 100 fs after the laser pulse is switched off. The shift in position of the C1-C2 *BCP* will be used as a scalar measure of the polarization effect because the C1-C2 *BCP* is positioned on the boundary of the C1 *NCP* and C2 *NCP*. The shift in the C1-C2 *BCP* caused by the laser pulse during the pulse and

after it is switched off is determined by calculating the relative partial bond-lengths and compared with relaxed ethene to give $\Delta(\text{C2-BCP}, \text{BCP-C1})$.

2.2 The QTAIM bond-path properties; the bond-path framework set \mathbb{B} and precession \mathbb{K}

The next-generation QTAIM [34] interpretation of the chemical bond is referred to as the *bond-path framework set*, denoted by \mathbb{B} , where $\mathbb{B} = \{\mathbf{p}, \mathbf{q}, \mathbf{r}\}$. Consequently, for a given electronic state \mathbb{B} comprises three ‘linkages’; \mathbf{p} , \mathbf{q} and \mathbf{r} associated with the \mathbf{e}_1 , \mathbf{e}_2 and \mathbf{e}_3 eigenvectors, respectively. The \mathbf{p} and \mathbf{q} , which are defined in 3-D space, are connectors which may not necessarily be linear since they may twist and intersect the bond-path. They are constructed from the least (\mathbf{e}_1) and most (\mathbf{e}_2) preferred directions of electronic charge density accumulation $\rho(\mathbf{r})$ along the bond-path, which is referred to as (\mathbf{r}) and is constructed from (\mathbf{e}_3). The $\{\mathbf{q}, \mathbf{q}'\}$ and $\{\mathbf{p}, \mathbf{p}'\}$ path-packets are scaled by the ellipticity ε due to the universal chemical interpretation of the ellipticity ε :

$$\begin{aligned} \mathbf{q}_i &= \mathbf{r}_i + \varepsilon_i \mathbf{e}_{2,i}, & \mathbf{q}'_i &= \mathbf{r}_i - \varepsilon_i \mathbf{e}_{2,i} \\ \mathbf{p}_i &= \mathbf{r}_i + \varepsilon_i \mathbf{e}_{1,i}, & \mathbf{p}'_i &= \mathbf{r}_i - \varepsilon_i \mathbf{e}_{1,i} \end{aligned} \quad (1)$$

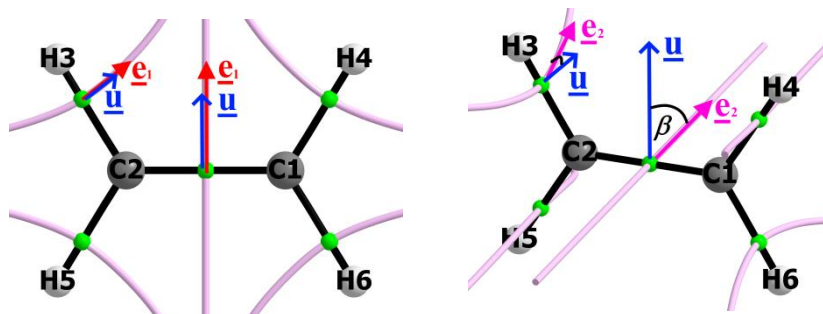
The orbital-like *packet* shapes that the pair of \mathbf{q} - and \mathbf{q}' -paths form along the *BCP* are referred to as a $\{\mathbf{q}, \mathbf{q}'\}$ path-packet. Extremely long $\{\mathbf{q}, \mathbf{q}'\}$ path-packets indicate the imminent *BCP* rupture. Larger $\{\mathbf{q}, \mathbf{q}'\}$ path-packets in the vicinity of a *BCP* signify an easier passage of the *BCP* as opposed to smaller $\{\mathbf{q}, \mathbf{q}'\}$ -path packets. The response of the $\{\mathbf{p}, \mathbf{p}'\}$ and $\{\mathbf{q}, \mathbf{q}'\}$ path-packets to an ultra-fast laser pulse in terms of the shape, symmetry, area and movement of the centre, i.e. the position of the *BCP*, of the $\{\mathbf{p}, \mathbf{p}'\}$ and $\{\mathbf{q}, \mathbf{q}'\}$ path-packets can all provide the NG-QTAIM interpretation of the response of the ultra-fast laser pulse.

We will now define the extent to which the $\{\mathbf{p}, \mathbf{p}'\}$ path-packet constructed from the \mathbf{e}_1 eigenvector wraps i.e. *precesses* about a bond-path, see the left panel of **Scheme 2**. For the $\{\mathbf{p}, \mathbf{p}'\}$ path-packet, defined by the \mathbf{e}_1 eigenvector, we wish to follow the extent to which the $\{\mathbf{p}, \mathbf{p}'\}$ path-packet precesses about the bond-path by defining the *precession* \mathbb{K} for bond-path-rigidity [44]–[46]:

$$\mathbb{K} = 1 - \cos^2 \alpha, \quad \text{where } \cos \alpha = \mathbf{e}_1 \cdot \mathbf{u} \quad \text{and} \quad 0 \leq \mathbb{K} \leq 1 \quad (2)$$

The reference direction \mathbf{u} is chosen to align maximally with the interatomic surface path (IAS) for the \mathbf{e}_1 eigenvector. Considering the extremes of \mathbb{K} , with α defined by equation (2), for $\mathbb{K} = 0$, there is maximum alignment of the reference direction \mathbf{u} with the \mathbf{e}_1 eigenvector, the least facile direction. For $\mathbb{K} = 1$ we have the maximum degree of alignment with the \mathbf{e}_2 eigenvector, the most facile direction. In other words, $\mathbb{K} = 0$ and $\mathbb{K} = 1$ indicate bond-paths with the lowest and highest tendencies towards bond-path-flexibility, respectively. The

precession \mathbb{K} is determined relative to the *BCP*, in either direction along the bond-path towards the nuclei at either end of the bond-path using an arbitrarily small spacing of \underline{e}_1 eigenvectors. If we choose the precession \mathbb{K} of the $\{p,p'\}$ path-packet about the bond-path when the $\pm \underline{e}_1$ eigenvector is parallel to \underline{u} , the *BCP* will have minimum facile character, i.e. bond-path-rigidity. By following the variation of the precession \mathbb{K} we can quantify the degree of facile character of a *BCP* along an entire bond-path.



Scheme 2. The construction of the $\{p,p'\}$ precession \mathbb{K} (left-panel) corresponding to the ethene molecular graph. The unit vectors \underline{u} (blue arrows) are defined as the reference directions for the C1-C2 *BCP* and the C2-H3 *BCP* and are parallel to the \underline{e}_1 eigenvectors (red arrows). The \mathbb{K} will be calculated for all bond-paths due to the directional nature of the applied ultra-fast laser pulse. The pale magenta lines indicate the interatomic surface paths (IAS) for the \underline{e}_1 eigenvectors that originate at a *BCP*. The green spheres indicate the locations of the *BCPs*. The $\{q,q'\}$ precession \mathbb{K}' (right-panel). The reference directions vectors \underline{u} (blue arrows) are shown for the reader's convenience and correspond to those in the left panel. The pale magenta lines indicate the IAS paths for the \underline{e}_2 eigenvectors that originate at a *BCP*.

The precession of the $\{q,q'\}$ path-packet, defined by the \underline{e}_2 eigenvector, about the bond-path, is defined by equation (3), see also **Scheme 2**:

$$\mathbb{K}' = 1 - \cos^2\beta, \text{ where } \cos\beta = \underline{e}_2 \cdot \underline{u}, \beta = (\pi/2 - \alpha) \text{ and } 0 \leq \mathbb{K}' \leq 1 \quad (3)$$

For $\mathbb{K}' = 0$ we have a maximum degree of facile character and for $\mathbb{K}' = 1$ we have the minimum degree of facile character. Values of the precession \mathbb{K}' in the range $0 \leq \mathbb{K}' \leq 1$ indicate polarization of the electron density distribution $\rho(\mathbf{r})$ associated with the bond-path in terms of the changing orientation of the \underline{e}_2 eigenvectors, from parallel to perpendicular, including intermediate orientations of the \underline{e}_2 eigenvector. Consequently, there will be a spectrum of 'mixed' bond types within the limits of the rigid shared-shell character $\mathbb{K}' = 1$, characteristic of pi-bonds, e.g. the C1-C2 bond of ethane, and flexible closed-shell character $\mathbb{K}' = 0$, characteristic of weaker closed-shell bonds that are more flexible, e.g. hydrogen bonds.

In this investigation, the integral, i.e. the area under the precession \mathbb{K}' , is calculated separately for the C1-*BCP* and *BCP*-C2 regions, and is referred to as Q_1 and Q_2 , respectively. The corresponding normalized areas $Q_{1\text{norm}} = Q_1/\text{PBPL}_1$, $Q_{2\text{norm}} = Q_2/\text{PBPL}_2$ will be calculated, where PBPL_1 is the partial bond-path length for the C1-*BCP*

portion C1-C2 *BCP* bond-path i.e. the path between the C1 atom and the *BCP* with similar for PBPL₂. The C1-C2 *BCP* motion is quantified by the \underline{e}_3 eigenvector that is directed along the C1-C2 *BCP* bond-path. The reason for obtaining the normalized $Q_{1\text{norm}}$ and $Q_{2\text{norm}}$ values is to remove the effect of C1-C2 *BCP* movement on the Q_1 and Q_2 values. This is because we want to quantify the directional changes to the chemical character using the \underline{e}_1 and \underline{e}_2 eigenvectors that are used to construct the precession \mathbb{K}' and the Q_1 and Q_2 values. The $Q_{1\text{norm}}$ and $Q_{2\text{norm}}$ values will provide a measure of the change in chemical character that can be compared to the molecular graph of the relaxed ethene, where higher and lower values indicate more rigid and less rigid C1-C2 *BCP* chemical character compared to the relaxed ethane, respectively. Differences in the magnitudes of the $Q_{1\text{norm}}$ and $Q_{2\text{norm}}$ values indicate polarization effects.

The normalized areas $Q_{1\text{norm}}$ and $Q_{2\text{norm}}$ will be calculated for each of the four laser pulse frequencies before and after the laser pulse is switched off.

3. Computational Details

A set of configuration state functions was computed to build pseudo-CI (configuration interaction) singles eigenvectors in the zero external electric (\mathbf{E}) field case, using the hybrid linear response time-dependent density functional theory/configuration interaction (LR-TDDFT/CI) approach detailed in previous work[47]–[49]. This was undertaken using TD-DFT at the CAM-B3LYP[50] /aug-cc-pVTZ[51], [52] level, both shown elsewhere in the literature[53] as providing accurate descriptions of excited states. The calculations were carried out using the Gaussian G09 v.E.01[54] package without symmetry constraints and using an ‘ultrafine’ integration grid, solving for the fifty lowest-energy excited states. Each time-independent many-electron state was formulated as a linear combination of singly-excited configuration state functions. Using the time-dependent CI implementation within the detCI module[47], [48] within the ORBKIT[55] package, a library of transition dipole moments between states was precomputed for use in propagating the electron dynamics within the clamped-nuclei approximation. The electron dynamics were propagated using the many-electron time dependent Schrödinger equation using the field-free Hamiltonian, within the Born-Oppenheimer approximation, with the additional semi-classical dipole approximation term $-\boldsymbol{\mu} \cdot \mathbf{E}(t)$, where the dot indicates a vector dot product, where $\boldsymbol{\mu}$ is the dipole operator and $\mathbf{E}(t)$ is the time-dependent applied electric field. The effect of arbitrarily applied non-ionizing ultrafast laser pulses was modelled by specifying the time dependence of the spatial components of $\mathbf{E}(t)$ along with their polarization and relative phase information using cubic spline interpolation between pre-calculated \mathbf{E} -field vs. time values. The pre-computed dipole moment library was used at each dynamics time-step to calculate the dipole interaction term $-\boldsymbol{\mu} \cdot \mathbf{E}(t)$. The wavefunction was propagated as a linear complex-weighted sum of the previously computed pseudo-CI singles states, as described in previous work[47], [48].

The electron dynamics were propagated for a total of 100 fs in the ‘interaction’ representation, applying a 20 fs ‘sine-squared’-shaped laser pulse of peak amplitude 200×10^{-4} a.u., polarized along the chosen x-axis of the molecule (along the C1-C2 bond), for a set of laser frequencies corresponding to a number of excitation energies spanning a range of the lower-lying excited states. A ‘field broadening’ approach is employed: for a ‘sin²’ amplitude envelope function pulse of duration ΔT , then the energetic broadening of the field is simply $\Delta E = \hbar/\Delta T$. Low-lying electronic states are usually well separated energetically, so only very short pulses, such as the 20fs pulse used here, are broad enough to excite the desired superposition states. The half-cycle ‘sin²’ envelope function of duration 20fs, which takes values in the range 0.0-1.0, describing the time dependence of the amplitude of the single pulse, is multiplied by the function $E_x \sin(\omega t)$ where ω is the chosen laser excitation frequency and E_x is the peak electric field magnitude in the x-direction along the C1-C2 bond, to give the overall time dependence of the simulated electric field. Both the sin² envelope function and the time dependent electric field $E_x \sin(\omega t)$ function commence at time $t = 0$ with a phase shift of 0. Short pulses are inherently energetically broad: they are inevitably unselective, so the set of excitation energies (i.e. field frequencies) are chosen to span a relatively wide range of the lower-lying excited states. More selective strategies for excitation of superposition states are elusive and are still being actively sought in the research literature, e.g. ‘undertuning’ and ‘overtuning’ strategies have had only mitigated success[56], although laser-induced selective alignment of molecules relative to fields is now experimentally possible[57], [58].

During the electron dynamics, snapshots of the total electronic charge density distribution $\rho(\mathbf{r})$ were generated as a ‘gridded’ scalar field with a grid spacing of 0.1 a.u. and a grid edge padding distance of 4.0 a.u. on all sides of the molecule. The CRITIC2 code[59] with the ‘density-smoothing’[60] option was used to obtain the bond critical points (BCPs), bond paths and eigenvectors of the Hessian of the density $\rho(\mathbf{r})$ for each snapshot, ensuring that the Poincaré-Hopf relationship was satisfied in all cases. NG-QTAIM properties were obtained using the in-house QuantVec[61] suite which is compatible with the CRITIC2 code. Visualization of molecular graphs and $\{q,q'\}$ and $\{p,p'\}$ path-packets was performed using the ‘topviz’ package within QuantVec employing the Mayavi[62] graphics toolkit.

Results and Discussion

In this investigation, we chose the highly symmetric planar ethene molecule to determine the QTAIM and NG-QTAIM properties arising from the application of a non-ionizing ultra-fast laser pulse with peak electric field $E_x = \pm 200.0 \times 10^{-4}$ a.u., see **Scheme 1**.

Four laser pulse frequencies $\omega = 0.2692$ a.u., 0.2808 a.u., 0.2830 a.u. and 0.2900 a.u. were chosen to correspond to excitation energies mid-way between the (S₁,S₂), (S₂,S₃), (S₃,S₄) and (S₄,S₅) electronic states, respectively, along with the associated electronic state populations, see **Supplementary Materials S1**. The corresponding variations with time of the laser pulse frequencies display positive and negative extrema of the E_x -field values,

which are both slightly shifted with respect to the peak of the laser pulse; see the **Supplementary Materials S2**. The tabulated partial bond-lengths and values of (Q_1 , Q_2) of the symmetry inequivalent C-H *BCPs* and relative C-H *BCP* shifts (compared to the relaxed ethene molecule) in *BCP* positions are provided in the **Supplementary Materials S3**. The partial bond-lengths C1-*BCP* and *BCP*-C2 of the C1-C2 *BCP* and the symmetry inequivalent and C-H *BCPs*, in the absence of the laser pulse, i.e. for the relaxed ethene molecule, are presented in **Table 1**. The areas under the C1-*BCP* (Q_1) and *BCP*-C2 (Q_2) portions of the precession \mathbb{K}' plot are presented in **Table 1**. The absence of polarization effect for the C1-C2 *BCP* is evident from the equal magnitude of Q_1 and Q_2 , which is due to the symmetrical positioning of the C1-C2 *BCP* mid-way between the C1 *NCP* and C2 *NCP*, see **Table 1**. The partial bond-lengths C1-*BCP*, *BCP*-C2, relative partial bond-lengths, i.e. compared with relaxed ethene, $\Delta(\text{C2-BCP}, \text{BCP-C1})$ and $Q_{1\text{norm}} = Q_1/\text{PBPL}_1$, $Q_{2\text{norm}} = Q_2/\text{PBPL}_2$ for the four frequencies and up to 100 fs after the pulse is switched off are also presented in **Tables 2-5**.

In this investigation, we only consider the Q_1 , Q_2 values associated with the C1-C2 *BCP* due to the symmetrical positioning of the C1-C2 *BCP* along the C1-C2 *BCP* bond-path in the relaxed ethene molecule. The precession \mathbb{K} , \mathbb{K}' plots for the C1-C2 *BCP* bond-paths are provided in the **Supplementary Materials S4**.

The $\{q, q'\}$ path-packets for the 20 fs duration of the laser pulse for the four frequencies $\omega = 0.2692$ a.u., 0.2808 a.u., 0.2830 a.u. and 0.2900 a.u. are presented in sub-figures (a-c) of **Figures 1-4** respectively. The corresponding $\{q, q'\}$ path-packets at 100 femtoseconds (fs) after the pulse is switched off are presented in the sub-figure (d) of **Figures 1-4**. The remaining $\{q, q'\}$ path-packets and corresponding $\{p, p'\}$ path-packets are presented in the **Supplementary Materials S5**.

For the lowest frequency $\omega = 0.2692$ a.u., which corresponds to an excitation energy mid-way between the S_1 and S_2 electronic states, the effect of the $+\mathbf{E}_x$ -field and $-\mathbf{E}_x$ -field directions are clearly visible for the C1-C2 *BCP* in the form of a tear drop shaped $\{q, q'\}$ path-packet with the pointed-to-blunt end being oriented $\text{C1} \leftarrow \text{C2}$ and $\text{C1} \rightarrow \text{C2}$ for the $+\mathbf{E}_x$ -field and $-\mathbf{E}_x$ -field directions, respectively, see sub-figures (a-c) of **Figure 1**. This finding is consistent with our previous results that quantified the C1-C2 *BCP* shift in ethene with a static $\pm\mathbf{E}_x$ -field [33]. The effect of the laser pulse is apparent 100 fs after the pulse is switched off by observing differences in the morphology of the $\{q, q'\}$ path-packets compared with the $\{q, q'\}$ path-packets of relaxed ethene, see the left panel of **Scheme 1**. In particular, the C1-C2 *BCP* $\{q, q'\}$ path-packet of relaxed ethene is completely symmetrical, and there are no differences in the C-H *BCP* $\{q, q'\}$ path-packets on the left and right hand side of the C1-C2 *BCP* bond-path. These directional effects are dependent on the $\pm\mathbf{E}_x$ -field and are not apparent for the laser pulses created from frequencies of $\omega = 0.2808$ a.u. and $\omega = 0.2830$ a.u.; instead the C1-C2 *BCP* $\{q, q'\}$ path-packets are narrower or wider depending on the time interval, see **Figures 2-3** respectively. It is also observed that differences in the electronic state populations for the frequencies $\omega = 0.2808$ a.u. and $\omega = 0.2830$ a.u. are very small and difficult to interpret. The corresponding C1-C2 *BCP* $\{q, q'\}$ path-packets however display significant differences, compare **Figure 2** and **Figure 3**. For the highest frequency considered ($\omega = 0.2900$ a.u.), the C1-C2 *BCP* $\{q, q'\}$

path-packets possess a superposition of tear drop forms dependent on the $\pm E_x$ -field and smaller/larger path-packets. Therefore, the C1-C2 *BCP* $\{q, q'\}$ path-packets for $\omega = 0.2900$ a.u. are intermediate in morphology between the lowest frequency $\omega = 0.2692$ a.u. and the intermediate frequencies $\omega = 0.2808$ a.u. and $\omega = 0.2830$ a.u.

Corresponding to the tear drop shaped C1-C2 *BCP* $\{q, q'\}$ path-packets for the lowest frequency $\omega = 0.2692$ a.u. for the duration of the laser pulse, there is a dependency on the direction of the C1-C2 *BCP* shift for the $\pm E_x$ -field direction, see **Table 2**. This is evident from the C1-C2 *BCP* movement towards the C2 *NCP* for the positive field $+E_x$ and away from the C2 *NCP* for the negative field $-E_x$. Note that the positive field $+E_x$ corresponds to the C1 \leftarrow C2 direction and the negative field $-E_x$ corresponds to the C1 \rightarrow C2 direction, see **Scheme 1**. Conversely, the lack of tear drop shaped C1-C2 *BCP* $\{q, q'\}$ path-packets during the pulse for the frequencies $\omega = 0.2808$ a.u. and $\omega = 0.2830$ a.u. lacks a clear dependency of the C1-C2 *BCP* movement on the $\pm E_x$ -field direction, see **Table 3** and **Table 4** respectively. This is also the case for the highest frequency $\omega = 0.2900$ a.u., see **Table 5**. After the pulse is switched off, the C1-C2 *BCP* shifts i.e. $\Delta(\text{C2-BCP}, \text{BCP-C1})$ reduce in magnitude, see **Table 2**. This reduced magnitude of C1-C2 *BCP* shift is still significantly larger than that of the previously published work [33] on ethene subjected to a static E_x -field $= \pm 200$ a.u., where values of $\Delta(\text{C1-BCP}, \text{BCP-C2}) = \pm 0.030$ a.u. For the remaining three frequencies, the C1-C2 *BCP* shifts increase in magnitude after the pulse is removed, see **Tables 3-5**. For all four frequencies, the C1-C2 *BCP* shifts were for practical purposes identical in magnitude for each portion of the bond-path, e.g. $\Delta(\text{C2-BCP} = 0.119 \text{ a.u.}, \text{BCP-C1} = -0.119 \text{ a.u.})$ for $+E_x$ -field $\approx \pm 200$ a.u., see **Table 2**. This is not the case for the directional chemical character along the C1-C2 *BCP* bond-path as measured by the $Q_{1\text{norm}}$ and $Q_{2\text{norm}}$ values. The effect of the laser pulse is to change the directional chemical character along the C1-C2 *BCP* bond-path as measured by the $Q_{1\text{norm}}$ and $Q_{2\text{norm}}$ values compared with the relaxed ethene (0.600, 0.600), see **Tables 2-5**. This is evident in the increased polarization of the $Q_{1\text{norm}}$ and $Q_{2\text{norm}}$ values for the lowest frequency ($\omega = 0.2692$ a.u.), e.g. for $+E_x$ -field $\approx \pm 200$ a.u. $Q_{1\text{norm}} = 0.422$ and $Q_{2\text{norm}} = 0.934$ and for the highest frequency ($\omega = 0.2900$ a.u.) $Q_{1\text{norm}} = 0.829$ and $Q_{2\text{norm}} = 0.431$, see **Table 2** and **Table 5**, respectively. Although this polarization of $Q_{1\text{norm}}$ and $Q_{2\text{norm}}$ values is not apparent for the intermediate frequencies, the $Q_{1\text{norm}}$ and $Q_{2\text{norm}}$ values are still distinguishable, e.g. $Q_{1\text{norm}} = 0.559$ and $Q_{2\text{norm}} = 0.642$. Conversely, after the pulse is switched off the $Q_{1\text{norm}}$ and $Q_{2\text{norm}}$ values remain about the same for the lowest frequency and tend to decrease for the three higher frequencies.

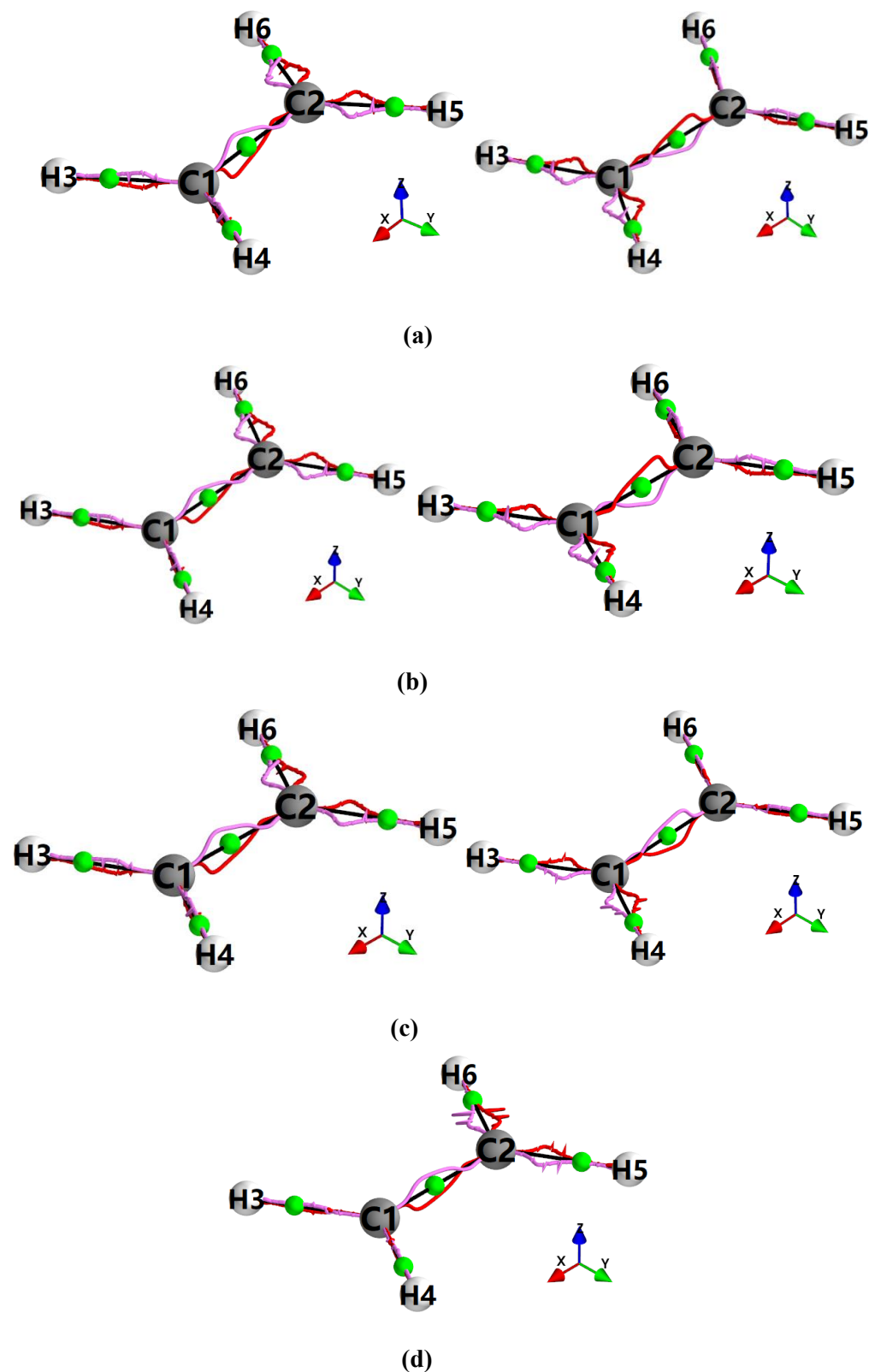


Figure 1. The ethene bond-path framework set \mathbb{B} displaying the $\{q$ (magenta), q' (red) $\}$ path-packets for values of the laser pulse frequency $\omega = 0.2692$ a.u. for $E_x = -98.2 \times 10^{-4}$ a.u. at time = 4.944 fs (left-panel) and $E_x = +107.0 \times 10^{-4}$ a.u. at time = 5.224 fs (right-panel) of sub-figure (a). The $\{q, q'\}$ path-packets corresponding to the peak $\pm E$ -field values: $E_x = -200.0 \times 10^{-4}$ a.u. (at 10.022 fs) and $E_x = +199.6 \times 10^{-4}$ a.u. (at 9.742 fs) are presented in the left and right panels respectively of sub-figure (b). The $\{q, q'\}$ path-packets for $E_x = -96.8 \times 10^{-4}$ a.u. (at 15.101 fs) and $E_x = +105.6 \times 10^{-4}$ a.u. (at 14.821 fs) are presented in the left and right panels respectively of sub-figure (c). The $\{q, q'\}$ path-packets at 100 fs after the pulse is switched off is presented in sub-figure (d). For further details see **scheme 1**.

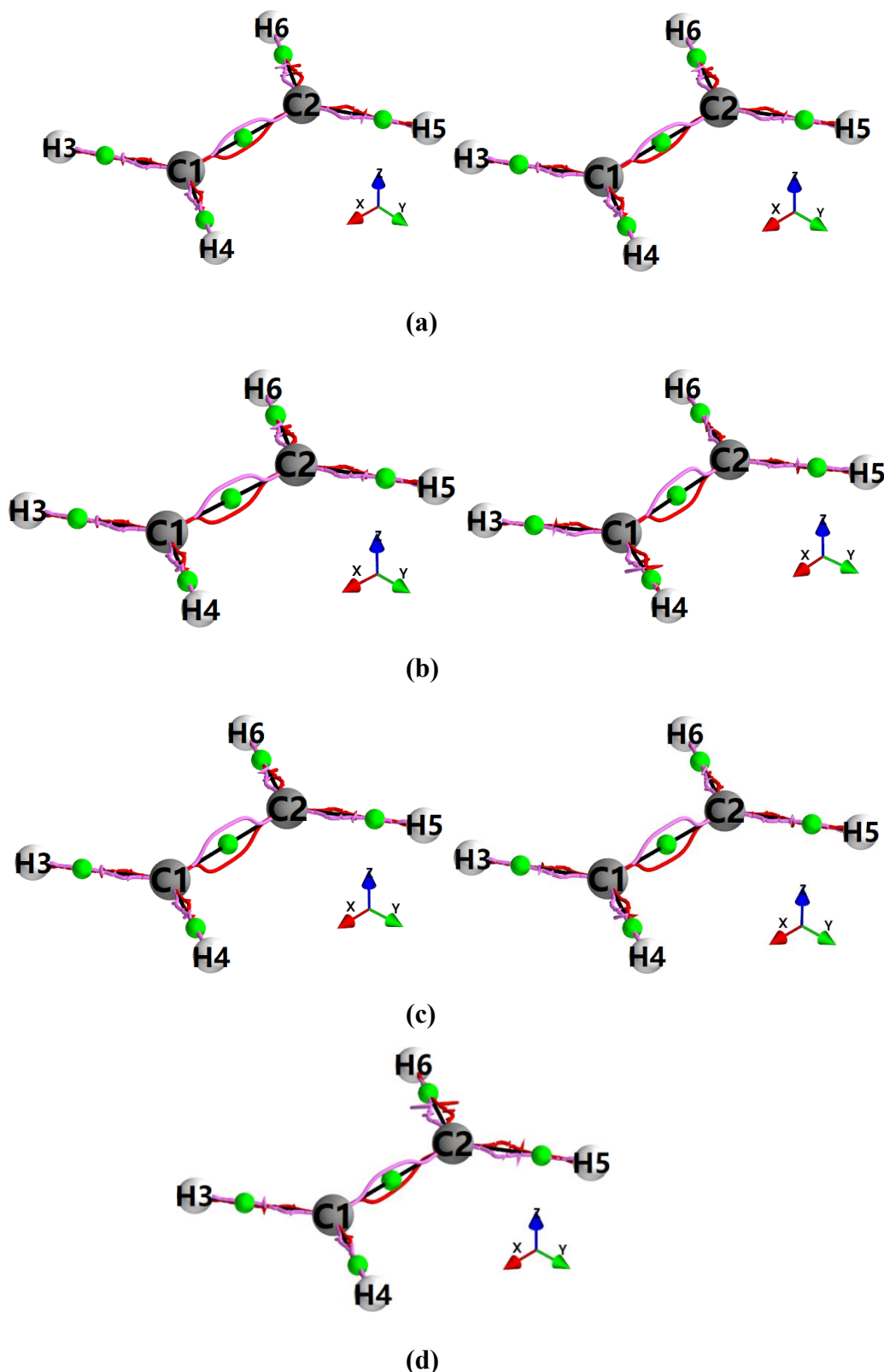


Figure 2. The ethene bond-path framework set \mathbb{B} displaying the $\{q$ (magenta), q' (red) $\}$ path-packets for values of the laser pulse frequency $\omega = 0.2808$ a.u. for $E_x = -91.7 \times 10^{-4}$ a.u. at time = 4.741 fs (left-panel) and $E_x = +100.2 \times 10^{-4}$ a.u. at time = 5.011 fs (right-panel) of sub-figure (a). The $\{q, q'\}$ path-packets corresponding to the peak $\pm E$ -field values: $E_x = -199.8 \times 10^{-4}$ a.u. (at 10.151 fs) and $E_x = +199.7 \times 10^{-4}$ a.u. (at 9.882 fs) are presented in the left and right panels respectively of sub-figure (b). The $\{q, q'\}$ path-packets for $E_x = -99.3 \times 10^{-4}$ a.u. (at 15.022 fs) and $E_x = +107.7 \times 10^{-4}$ a.u. (at 14.752 fs) are presented in the left and right panels respectively of sub-figure (c). The $\{q, q'\}$ path-packets at 100 fs after the pulse is switched off is presented in sub-figure (d). For further details see **scheme 1**.

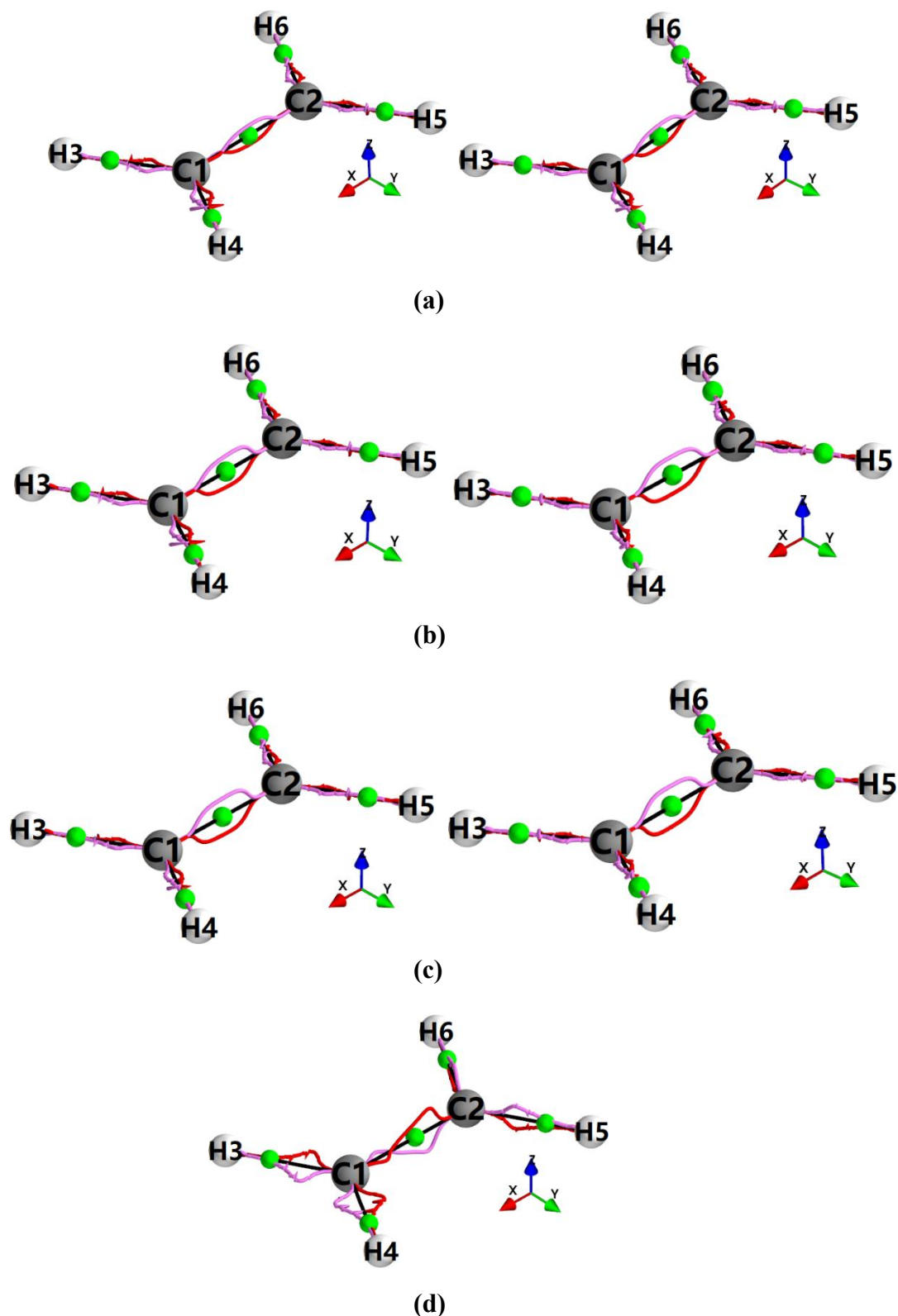


Figure 3. The ethene bond-path framework set \mathbb{B} displaying the $\{q$ (magenta), q' (red) $\}$ path-packets for values of the laser pulse frequency $\omega = 0.2830$ a.u. for $E_x = -107.4 \times 10^{-4}$ a.u. at time = 5.235 fs (left-panel) and $E_x = +99.0 \times 10^{-4}$ a.u. at time = 4.968 fs (right-panel) of sub-figure (a). The $\{q, q'\}$ path-packets corresponding to the peak $\pm E$ -field values: $E_x = -199.6 \times 10^{-4}$ a.u. (at 10.064 fs) and $E_x = +199.6 \times 10^{-4}$ a.u. (at 9.797 fs) are presented in the left and right panels, respectively of sub-figure (b). The $\{q, q'\}$ path-packets for $E_x = -103.0 \times 10^{-4}$ a.u. (at 14.904 fs) and $E_x = +94.6 \times 10^{-4}$ a.u. (at 15.171 fs) are presented in the left and right panels respectively of sub-figure (c). The $\{q, q'\}$ path-packets at 100 fs after the pulse is switched off is presented in sub-figure (d). For further details see **scheme 1**.

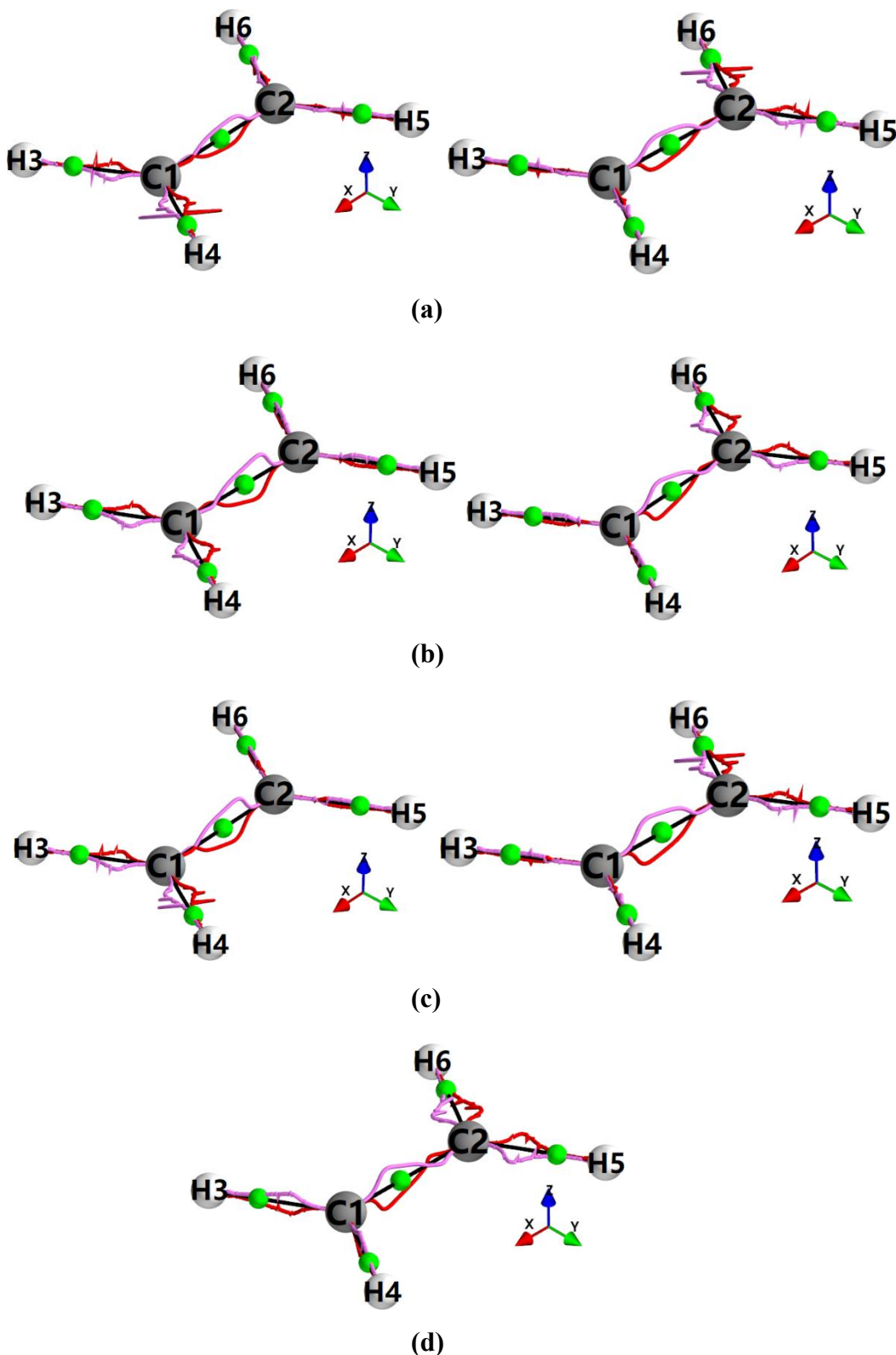


Figure 4. The ethene bond-path framework set \mathbb{B} displaying the $\{q$ (magenta), q' (red) $\}$ path-packets for values of the laser pulse frequency $\omega = 0.290$ a.u. for $E_x = -103.4 \times 10^{-4}$ a.u. at time = 5.115 fs (left-panel) and $E_x = +95.1 \times 10^{-4}$ a.u. at time = 4.854 fs (right-panel) of sub-figure (a). The $\{q, q'\}$ path-packets corresponding to the peak $\pm E$ -field values: $E_x = -199.7 \times 10^{-4}$ a.u. (at 9.823 fs) and $E_x = +199.6 \times 10^{-4}$ a.u. (at 10.083 fs) are presented in the left and right panels respectively of sub-figure (b). The $\{q, q'\}$ path-packets for $E_x = -97.9 \times 10^{-4}$ a.u. (at 15.062 fs) and $E_x = +106.1 \times 10^{-4}$ a.u. (at 14.802 fs) are presented in the left and right panels respectively of sub-figure (c). The $\{q, q'\}$ path-packets at 100 fs after the pulse is switched off is presented in sub-figure (d). For further details see **scheme 1**.

Table 1. Values of the partial bond-path lengths (BPL) in a.u., in the absence of an electric field. Q_1 corresponds to the area under the precession \mathbb{K}' plot from C1 to the BCP, Q_2 corresponds to the area under the precession \mathbb{K}' plot from the BCP to C2 in atomic units (a.u.). $Q_{1\text{norm}} = Q_1/\text{PBPL}_1$, $Q_{2\text{norm}} = Q_2/\text{PBPL}_2$.

Time (fs)	$\pm E_x$	C2-BCP, BCP-C1	(Q_1, Q_2)	$(Q_{1\text{norm}}, Q_{2\text{norm}})$
0.0	---	1.2377, 1.2377	(0.743, 0.743)	(0.600, 0.600)

Table 2. Values of the partial bond-path lengths C1-BCP, BCP-C2 and C1-C2 BCP shifts $\Delta(\text{C1-BCP}, \text{BCP-C2})$ for ethene subject to a laser pulse of duration 20 fs with frequency $\omega = 0.2692$ a.u. The laser pulse electric field E_x was directed along the bond-path with units of $\times 10^{-4}$ a.u., see the caption of **Table 1** and **Scheme 1** for further details.

$\omega = 0.2692$ a.u.				
Pulse (fs)	$\pm E_x$	C1-BCP, BCP-C2	$\Delta(\text{C1-BCP}, \text{BCP-C2})$	$(Q_{1\text{norm}}, Q_{2\text{norm}})$
5.224	+107.0	1.352, 1.123	(0.114, -0.114)	(0.395, 0.914)
4.944	-98.2	1.122, 1.354	(-0.116, 0.116)	(0.914, 0.409)
9.742	+199.6	1.357, 1.119	(0.119, -0.119)	(0.422, 0.934)
10.022	-200.0	1.127, 1.349	(-0.111, 0.111)	(0.910, 0.396)
14.821	+105.6	1.318, 1.157	(0.081, -0.081)	(0.449, 0.772)
15.101	-96.8	1.132, 1.343	(-0.105, 0.105)	(0.906, 0.426)
After pulse (fs)				
20.0	---	1.153, 1.322	(-0.084, 0.084)	(0.742, 0.480)
40.0	---	1.139, 1.336	(-0.099, 0.099)	(0.834, 0.480)
60.0	---	1.164, 1.311	(-0.073, 0.073)	(0.719, 0.503)
80.0	---	1.193, 1.283	(-0.045, 0.045)	(0.622, 0.508)
100.0	---	1.169, 1.307	(-0.069, 0.069)	(0.700, 0.480)

Table 3. Values of the partial bond-path lengths C1-BCP, BCP-C2 and C1-C2 BCP shifts $\Delta(\text{C1-BCP}, \text{BCP-C2})$ and $Q_{1\text{norm}}$, $Q_{2\text{norm}}$ in the presence of an electric field E_x during the application of the ultra-fast laser pulse with frequency $\omega = 0.2808$ a.u. and after the pulse is removed, see **Table 2** for further details.

$\omega = 0.2808$ a.u.				
Pulse (fs)	$\pm E_x$	C1-BCP, BCP-C2	$\Delta(\text{C1-BCP}, \text{BCP-C2})$	$(Q_{1\text{norm}}, Q_{2\text{norm}})$
5.011	+100.2	1.230, 1.246	(-0.008, 0.008)	(0.527, 0.490)
4.741	-91.7	1.222, 1.253	(-0.015, 0.015)	(0.561, 0.502)
9.882	+199.7	1.260, 1.215	(0.022, -0.022)	(0.559, 0.642)
10.151	-199.8	1.230, 1.245	(-0.008, 0.008)	(0.573, 0.551)
14.752	+107.7	1.247, 1.228	(0.009, -0.009)	(0.580, 0.620)
15.022	-99.3	1.229, 1.247	(-0.009, 0.009)	(0.620, 0.580)
20.0	---	1.068, 1.408	(-0.170, 0.170)	(0.978, 0.366)
40.0	---	1.070, 1.406	(-0.168, 0.168)	(0.976, 0.367)
60.0	---	1.101, 1.375	(-0.137, 0.137)	(0.983, 0.389)
80.0	---	1.166, 1.309	(-0.072, 0.072)	(0.702, 0.423)
100.0	---	1.205, 1.270	(-0.033, 0.032)	(0.585, 0.466)

Table 4. Values of the partial bond-path lengths $C1-BCP$, $BCP-C2$ and $C1-C2$ BCP shifts $\Delta(C1-BCP, BCP-C2)$ and Q_{1norm} , Q_{2norm} in the presence of an electric field E_x during the application of the ultra-fast laser pulse with frequency $\omega = 0.2830$ a.u. and after the pulse is removed, see **Table 2** for further details.

$\omega = 0.2830$ a.u.				
Pulse (fs)	$\pm E_x$	$C1-BCP, BCP-C2$	$\Delta(C1-BCP, BCP-C2)$	(Q_{1norm}, Q_{2norm})
4.968	+99.0	1.249, 1.226	(0.012, -0.012)	(0.498, 0.529)
5.235	-107.4	1.254, 1.222	(0.016, -0.016)	(0.456, 0.515)
9.797	+199.6	1.233, 1.242	(-0.004, 0.004)	(0.602, 0.583)
10.064	-199.6	1.256, 1.219	(0.019, -0.019)	(0.546, 0.609)
15.171	+94.6	1.231, 1.244	(-0.006, 0.006)	(0.619, 0.597)
14.904	-103.0	1.247, 1.228	(0.009, -0.009)	(0.580, 0.620)
20.0	---	1.189, 1.286	(-0.048, 0.048)	(0.656, 0.445)
40.0	---	1.256, 1.220	(0.018, -0.018)	(0.486, 0.547)
60.0	---	1.325, 1.150	(0.088, -0.088)	(0.418, 0.761)
80.0	---	1.378, 1.098	(0.140, -0.140)	(0.388, 0.985)
100.0	---	1.385, 1.091	(0.147, -0.147)	(0.372, 0.974)

Table 5. Values of the partial bond-path lengths $C1-BCP$, $BCP-C2$ and $C1-C2$ BCP shifts $\Delta(C1-BCP, BCP-C2)$ and Q_{1norm} , Q_{2norm} in the presence of an electric field E_x during the application of the ultra-fast laser pulse with frequency $\omega = 0.2900$ a.u. and after the pulse is removed, see **Table 2** for further details.

$\omega = 0.2900$ a.u.				
Pulse (fs)	$\pm E_x$	$C1-BCP, BCP-C2$	$\Delta(C1-BCP, BCP-C2)$	(Q_{1norm}, Q_{2norm})
4.854	+95.1	1.189, 1.286	(-0.048, 0.048)	(0.656, 0.460)
5.115	-103.4	1.284, 1.191	(0.046, -0.046)	(0.446, 0.623)
10.083	+199.6	1.147, 1.328	(-0.091, 0.091)	(0.829, 0.431)
9.823	-199.7	1.329, 1.147	(0.091, -0.091)	(0.459, 0.845)
14.802	+106.1	1.177, 1.299	(-0.061, 0.061)	(0.743, 0.499)
15.062	-97.9	1.310, 1.165	(0.073, -0.073)	(0.495, 0.800)
20.0	---	1.120, 1.355	(-0.118, 0.118)	(0.916, 0.381)
40.0	---	1.090, 1.385	(-0.148, 0.148)	(0.975, 0.359)
60.0	---	1.064, 1.411	(-0.174, 0.174)	(0.981, 0.366)
80.0	---	1.072, 1.404	(-0.166, 0.166)	(0.974, 0.367)
100.0	---	1.102, 1.374	(-0.136, 0.136)	(0.982, 0.375)

Conclusions

Next generation QTAIM was used to quantify the electron dynamics arising from the application of an ultra-fast non-ionizing laser pulse of duration 20 fs, with peak amplitude $\pm E_x = 200 \times 10^{-4}$ a.u. directed along the ethene C1-C2 *BCP* bond-path. Four laser pulse frequencies $\omega = 0.2692$ a.u., 0.2808 a.u., 0.2830 a.u. and 0.2900 a.u., were chosen to correspond to excitation energies mid-way between the (S₁,S₂), (S₂,S₃), (S₃,S₄) and (S₄,S₅) electronic states, respectively. The after effects of the laser pulse, up to 100 fs after the laser pulse was switched off, on the total electronic charge density distribution $\rho(\mathbf{r})$ were also quantified.

The scalar QTAIM measures were used to quantify the C1-C2 *BCP* shifts, but were not able to distinguish the directional effects induced by the $+E_x$ and $-E_x$ directions of the laser pulse since all the C1-C2 *BCP* shifts possessed identical magnitudes for the $\pm E_x$ directions.

The directional chemical measures in the form of the NG-QTAIM interpretation of chemical bonding, i.e. the C1-C2 *BCP* $\{q, q'\}$ path-packets, were used to visualize any polarization effects induced by the application of the laser pulse. Polarization effects were clearly evident for the lowest and highest C1-C2 *BCP* $\{q, q'\}$ path-packets in the form of tear drop shapes corresponding to the direction, $+E_x$ or $-E_x$, of the laser pulse. These polarization effects increased, in the form of more pronounced tear drop shaped $\{q, q'\}$ path-packets, after the laser pulse was switched off for the laser pulse frequencies $\omega = 0.2808$ a.u. and 0.2900 a.u. The C-H *BCPs* did not align parallel/anti-parallel to the E_x orientation of the applied laser pulse. The response of the $\{q, q'\}$ path-packets is strongly asymmetric depending on the direction of the $+E_x$ or $-E_x$ laser pulse and stronger than for the static $\pm E_x$ -field with the same magnitude 200×10^{-4} a.u. The $\{q, q'\}$ path-packets were quantified in the form of the precession \mathbb{K}' plots; the area under these \mathbb{K}' plots was normalized to remove the effect of the *BCP* sliding, resulting in $Q_{1\text{norm}}$ and $Q_{2\text{norm}}$ values. The $Q_{1\text{norm}}$ and $Q_{2\text{norm}}$ values could be compared directly with the relaxed ethene molecule to provide an understanding of the laser-pulse-induced changes to the directional chemical character for the duration of the laser pulse and after the laser pulse was switched off. Comparison of the magnitudes of the $Q_{1\text{norm}}$ and $Q_{2\text{norm}}$ values with that of the relaxed ethene indicated increases and decreases in the strength, i.e. bond-rigidity vs bond-flexibility, of the C1-*BCP* and *BCP*-C2 bond-path sections. The strongest, i.e. most rigid, section of the C1-C2 *BCP* bond-path was the C1-*BCP* on account of possessing the highest values of $Q_{1\text{norm}}$ or $Q_{2\text{norm}}$ that occurred after the pulse was switched off for $\omega = 0.2808$ a.u. and 0.2900 a.u.

Differences in the magnitudes of the $Q_{1\text{norm}}$ and $Q_{2\text{norm}}$ values indicated polarization effects on a chemical bonding range that spanned strong (rigid) pi-character to weak (flexible) hydrogen bond-like interactions. Large effects were detected up to 100 fs after the laser pulse was switched off. These effects were stronger (more rigid) than those induced whilst the laser pulse was switch on.

The ability of NG-QTAM to provide analysis of the effects of an applied non-ionizing ultra-fast laser pulse without consideration of the nuclear dynamics highlights the sensitivity of NG-QTAIM to determine subtle

directional effects present in the electron dynamics. No other methods currently exist to provide these directional insights into the electron dynamics. NG-QTAIM is therefore of particular relevance for use with ultra-fast phenomena since nuclei respond orders of magnitude slower than the total electronic charge density distribution $\rho(\mathbf{r})$.

Conflict of Interests Statement

The authors have no conflict of interests to declare.

Funding Information

The Hunan Natural Science Foundation of China project gratefully acknowledged approval number: 2022JJ30029. The One Hundred Talents Foundation of Hunan Province is also gratefully acknowledged for the support of S.J. and S.R.K. H.F. and T.v.M. gratefully acknowledge computational support via the EaStCHEM Research Computing Facility.

Acknowledgements

The authors would like to acknowledge useful discussions with Jean-Christophe Tremblay, University of Lorraine, France.

References

- [1] G. E. Moore, *Proceedings of the IEEE*, **1998**, DOI:10.1109/JPROC.1998.658762.
- [2] M. A. Ratner, *Materials Today*, **2002**, DOI:10.1016/S1369-7021(02)05226-4.
- [3] Y. Komoto, S. Fujii, M. Iwane, M. Kiguchi, *J. Mater. Chem. C*, **2016**, DOI:10.1039/C6TC03268K.
- [4] R. E. Martin, F. Diederich, *Angewandte Chemie International Edition*, **1999**, DOI:10.1002/(SICI)1521-3773(19990517)38:10<1350::AID-ANIE1350>3.0.CO;2-6.
- [5] G. Mazur, R. Włodarczyk, *Journal of Computational Chemistry*, **2009**, DOI:10.1002/jcc.21102.
- [6] D. Nozaki, W. G. Schmidt, *Journal of Computational Chemistry*, **2017**, DOI:10.1002/jcc.24812.
- [7] A. Al-Backri, V. Zólyomi, C. J. Lambert, *J. Chem. Phys.*, **2014**, DOI:10.1063/1.4867635.
- [8] A. Moneo, A. González-Orive, S. Bock, M. Fenero, I. L. Herrero, D. C. Milan, M. Lorenzoni, R. J. Nichols, P. Cea, F. Perez-Murano, P. J. Low, S. Martin, *Nanoscale*, **2018**, DOI:10.1039/C8NR02347F.
- [9] W. Xu, E. Leary, S. Hou, S. Sangtarash, M. T. González, G. Rubio-Bollinger, Q. Wu, H. Sadeghi, L. Tejerina, K. E. Christensen, N. Agraït, S. J. Higgins, C. J. Lambert, R. J. Nichols, H. L. Anderson, *Angewandte Chemie International Edition*, **2019**, DOI:10.1002/anie.201901228.
- [10] H. Xing, A. Azizi, R. Momen, T. Xu, S. R. Kirk, S. Jenkins, *Int. J. Quantum Chem.*, **2022**, DOI:10.1002/qua.26884.
- [11] T. Mori, W. J. Glover, M. S. Schuurman, T. J. Martinez, *J. Phys. Chem. A*, **2012**, DOI:10.1021/jp2097185.
- [12] M. Ben-Nun, T. J. Martínez, *Chemical Physics Letters*, **1998**, DOI:10.1016/S0009-2614(98)01115-4.
- [13] T. J. Martínez, *Acc. Chem. Res.*, **2006**, DOI:10.1021/ar040202q.
- [14] B. G. Levine, T. J. Martínez, *Annu Rev Phys Chem*, **2007**, DOI:10.1146/annurev.physchem.57.032905.104612.
- [15] A. J. Merer, R. S. Mulliken, *Chem. Rev.*, **1969**, DOI:10.1021/cr60261a003.
- [16] J. Ryu, B. S. Hudson, *Chemical Physics Letters*, **1995**, DOI:10.1016/0009-2614(95)01017-4.
- [17] K. K. Baeck, T. J. Martinez, *Chemical Physics Letters*, **2003**, DOI:10.1016/S0009-2614(03)00847-9.
- [18] B. Sellner, M. Barbatti, T. Mueller, W. Domcke, H. Lischka, *Molecular Physics*, **2013**, DOI:10.1080/00268976.2013.813590.
- [19] E. G. Champenois, N. H. Shivaram, T. W. Wright, C.-S. Yang, A. Belkacem, J. P. Cryan, *J Chem Phys*, **2016**,

DOI:10.1063/1.4939220.

- [20] H. Tao, T. K. Allison, T. W. Wright, A. M. Stooke, C. Khurmi, J. van Tilborg, Y. Liu, R. W. Falcone, A. Belkacem, T. J. Martinez, *J Chem Phys*, **2011**, DOI:10.1063/1.3604007.
- [21] V. Stert, H. Lippert, H.-H. Ritze, W. Radloff, *Chemical Physics Letters*, **2004**, DOI:10.1016/j.cplett.2004.02.077.
- [22] T. K. Allison, H. Tao, W. J. Glover, T. W. Wright, A. M. Stooke, C. Khurmi, J. van Tilborg, Y. Liu, R. W. Falcone, T. J. Martinez, A. Belkacem, *J Chem Phys*, **2012**, DOI:10.1063/1.3697760.
- [23] K. Kosma, S. A. Trushin, W. Fuss, W. E. Schmid, *J Phys Chem A*, **2008**, DOI:10.1021/jp803548c.
- [24] T. Kobayashi, T. Horio, T. Suzuki, *J. Phys. Chem. A*, **2015**, DOI:10.1021/acs.jpca.5b06094.
- [25] A. Saenz, *Physical Review A*, **2000**, DOI:10.1103/PhysRevA.61.051402.
- [26] A. Saenz, *Physical Review A*, **2002**, DOI:10.1103/PhysRevA.66.063407.
- [27] Z. Medin, D. Lai, *Phys. Rev. A*, **2006**, DOI:10.1103/PhysRevA.74.062508.
- [28] S. Petretti, Y. V. Vanne, A. Saenz, A. Castro, P. Decleva, *Phys. Rev. Lett.*, **2010**, DOI:10.1103/PhysRevLett.104.223001.
- [29] S. Shaik, D. Mandal, R. Ramanan, *Nature Chemistry*, **2016**, DOI:10.1038/nchem.2651.
- [30] S. Shaik, R. Ramanan, D. Danovich, D. Mandal, *Chem. Soc. Rev.*, **2018**, DOI:10.1039/C8CS00354H.
- [31] Z. Wang, D. Danovich, R. Ramanan, S. Shaik, *J. Am. Chem. Soc.*, **2018**, DOI:10.1021/jacs.8b08233.
- [32] S. Sowlati-Hashjin, C. F. Matta, *J. Chem. Phys.*, **2013**, DOI:10.1063/1.4820487.
- [33] A. Azizi, R. Momen, H. Früchtl, T. van Mourik, S. R. Kirk, S. Jenkins, *J Comput Chem*, **2020**, DOI:10.1002/jcc.26137.
- [34] S. R. Kirk, S. Jenkins, *WIREs Comput. Mol. Sci.*, **2022**, DOI:10.1002/wcms.1611.
- [35] R. S. Judson, H. Rabitz, *Phys. Rev. Lett.*, **1992**, DOI:10.1103/PhysRevLett.68.1500.
- [36] M. Yu. Ivanov, D. R. Matusek, J. S. Wright, *Phys. Rev. A*, **1996**, DOI:10.1103/PhysRevA.54.5159.
- [37] M. Dantus, V. V. Lozovoy, *Chem. Rev.*, **2004**, DOI:10.1021/cr020668r.
- [38] A. D. Bandrauk, E.-W. S. Sedik, C. F. Matta, *Molecular Physics*, **2006**, DOI:10.1080/00268970500273983.
- [39] A. A. Arabi, C. F. Matta, *Phys. Chem. Chem. Phys.*, **2011**, DOI:10.1039/C1CP20175A.
- [40] W. J. Huang, T. Xu, S. R. Kirk, S. Jenkins, *Chem. Phys. Lett.*, **2018**, DOI:10.1016/j.cplett.2018.08.059.
- [41] R. F. W. Bader, in *Atoms in Molecules: A Quantum Theory*; Oxford University Press, USA, , **1994**.
- [42] R. F. W. Bader, *J. Phys. Chem. A*, **1998**, DOI:10.1021/jp981794v.
- [43] R. F. W. Bader, *J. Phys. Chem. A*, **2009**, DOI:10.1021/jp906341r.
- [44] Y. Yang, T. Xu, S. R. Kirk, S. Jenkins, *International Journal of Quantum Chemistry*, **2021**, DOI:10.1002/qua.26584.
- [45] X. Nie, Y. Yang, T. Xu, S. R. Kirk, S. Jenkins, *International Journal of Quantum Chemistry*, **2021**, DOI:10.1002/qua.26527.
- [46] B. Mahara, A. Azizi, Y. Yang, M. Filatov, S. R. Kirk, S. Jenkins, *Chemical Physics Letters*, **2021**, DOI:10.1016/j.cplett.2021.138339.
- [47] V. Pohl, G. Hermann, J. C. Tremblay, *Journal of Computational Chemistry*, **2017**, DOI:10.1002/jcc.24792.
- [48] G. Hermann, V. Pohl, J. C. Tremblay, *Journal of Computational Chemistry*, **2017**, DOI:10.1002/jcc.24896.
- [49] S. Giri, A. M. Dudzinski, J. C. Tremblay, G. Dixit, *Phys. Rev. A*, **2020**, DOI:10.1103/PhysRevA.102.063103.
- [50] T. Yanai, D. P. Tew, N. C. Handy, *Chemical Physics Letters*, **2004**, DOI:10.1016/j.cplett.2004.06.011.
- [51] R. A. Kendall, T. H. Dunning, R. J. Harrison, *J. Chem. Phys.*, **1992**, DOI:10.1063/1.462569.
- [52] T. H. Dunning, *J. Chem. Phys.*, **1989**, DOI:10.1063/1.456153.
- [53] R. Sarkar, M. Boggio-Pasqua, P.-F. Loos, D. Jacquemin, *J. Chem. Theory Comput.*, **2021**, DOI:10.1021/acs.jctc.0c01228.
- [54] Michael J. Frisch, G. W. Trucks, H. Bernhard Schlegel, Gustavo E. Scuseria, Michael A. Robb, James R. Cheeseman, Giovanni Scalmani, Vincenzo Barone, Benedetta Mennucci, G. A. Petersson, H. Nakatsuji, M. Caricato, Xiaosong Li, H. P. Hratchian, Artur F. Izmaylov, Julien Bloino, G. Zheng, J. L. Sonnenberg, M. Hada, M. Ehara, K. Toyota, R. Fukuda, J. Hasegawa, M. Ishida, T. Nakajima, Y. Honda, O. Kitao, H. Nakai, T. Vreven, J. A. Montgomery Jr., J. E. Peralta, François Ogliaro, Michael J. Bearpark, Jochen Heyd, E. N. Brothers, K. N. Kudin, V. N. Staroverov, Rika Kobayashi, J. Normand, Krishnan Raghavachari, Alistair P. Rendell, J. C. Burant, S. S. Iyengar, Jacopo Tomasi, M. Cossi, N. Rega, N. J. Millam, M. Klene, J. E. Knox, J. B. Cross, V. Bakken, C. Adamo, J. Jaramillo, R. Gomperts, R. E. Stratmann, O. Yazyev, A. J. Austin, R. Cammi, C. Pomelli, J. W. Ochterski, R. L. Martin, K. Morokuma, V. G. Zakrzewski, G. A. Voth, P. Salvador, J. J. Dannenberg, S. Dapprich, A. D. Daniels, Ö. Farkas, J. B. Foresman, J. V. Ortiz, J. Cioslowski, D. J. Fox, Gaussian 09, Revision E.01. Gaussian, Inc., 340 Quinnipiac St Bldg 40 Wallingford, CT 06492 USA, 2009.
- [55] G. Hermann, V. Pohl, J. C. Tremblay, B. Paulus, H.-C. Hege, A. Schild, *Journal of Computational Chemistry*, **2016**, DOI:10.1002/jcc.24358.
- [56] G. Füchsel, J. C. Tremblay, T. Klamroth, P. Saalfrank, *Israel Journal of Chemistry*, **2012**, DOI:10.1002/ijch.201100097.
- [57] I. Tutunnikov, E. Gershnel, S. Gold, I. Sh. Averbukh, *J. Phys. Chem. Lett.*, **2018**, DOI:10.1021/acs.jpclett.7b03416.
- [58] I. Tutunnikov, J. Floß, E. Gershnel, P. Brumer, I. Sh. Averbukh, A. A. Milner, V. Milner, *Phys. Rev. A*, **2020**, DOI:10.1103/PhysRevA.101.021403.
- [59] A. Otero-de-la-Roza, E. R. Johnson, V. Luaña, *Computer Physics Communications*, **2014**, DOI:10.1016/j.cpc.2013.10.026.
- [60] A. Otero-de-la-Roza, *The Journal of Chemical Physics*, **2022**, DOI:10.1063/5.0090232.
- [61] S. R. Kirk, S. Jenkins, QuantVec. BEACON Research Group, College of Chemistry and Chemical Engineering, Hunan Normal University, Changsha, Hunan, P.R. China, 2021.
- [62] P. Ramachandran, G. Varoquaux, *Computing in Science Engineering*, **2011**, DOI:10.1109/MCSE.2011.35.

